

# Simultaneously enhancing strength and ductility of HCP titanium via multi-modal grain induced extra $\langle c+a \rangle$ dislocation hardening

Lei Gu, Ao Meng, Xiang Chen<sup>\*</sup>, Yonghao Zhao<sup>\*</sup>

Nano and Heterogeneous Materials Center, School of Materials Science and Engineering, Nanjing University of Science and Technology, Nanjing 210094, China

## ARTICLE INFO

### Keywords:

multi-modal Ti  
strength and ductility  
hetero-deformation induced (HDI) hardening  
( $c + a$ ) dislocation

## ABSTRACT

According to Considère necking criterion, enhancing strength of a material will decrease its elongation to failure, i.e. ductility, even if the strain hardening rate remains unchanged. Unfortunately, four traditional strengthening mechanisms including grain refinement, deformation, solid solution and 2<sup>nd</sup>-phase particle strengthening increase the yield strength by increasing the critical shear stress for slip initiation and unexceptionally reduce the strain hardening ability and ductility. Recent experiments revealed that implementation of heterostructures can produce extra hetero-deformation induced (HDI) hardening and thus reduce ductility loss while enhancing strength. However, the improved ductility was still less than that of coarse-grained counterparts. Here we fabricated a bulk heterostructured Ti with a uniform multi-modal grain size distribution in which the single individual micro-grain is surrounded and constrained by three-dimensional ultrafine grains. Tensile tests revealed the multi-modal Ti has a high yield strength of 800 MPa, ductility of 28.5%, and outstanding HDI hardening effect compared with its coarse-grained counterparts (a yield strength of 550 MPa and ductility of 26.5%). These mechanical properties of our multi-modal Ti are also superior to other literature reported data of heterostructured Ti. Microstructural characterization further reveals the uniform distribution between hard and soft domains produces maximum interface density and HDI hardening effect. Moreover, the HDI causes extra ( $c + a$ ) geometrically necessary dislocations piling ups in the constrained micro-grains, which produce enough and extra strain hardening to maintain and even enhance slightly the ductility. Our work provides a strategy to simultaneously enhance strength and ductility of metals via enough and extra strain hardening capability increase.

## 1. Introduction

The rapid development of modern industry puts forward more and more stringent requirements for the comprehensive performance of materials, and these requirements often exceed the performance limits of the materials themselves. In this context, people have to search and design super materials with super comprehensive properties. Specifically, Ti and its alloys used in aerospace are required to simultaneously have excellent comprehensive properties such as high strength and high ductility, etc. High strength can help to improve energy efficiency and carbon neutrality, and high ductility is critical to safety and reliability of the aerospace parts, because it can avoid catastrophic fracture failure. However, strength and ductility are often a trade-off with each other, which bring challenges to Ti alloys used in aerospace.

In tensile tests, the onset of localized deformation, i.e., necking instability, is predicted by the Considère criterion [1] as:

$$\left(\frac{\partial\sigma}{\partial\varepsilon}\right)_{\varepsilon} \leq \sigma \quad (1)$$

where  $\sigma$  and  $\varepsilon$  are true stress and true strain, respectively, and  $\dot{\varepsilon}$  is the strain rate.  $\partial\sigma/\partial\varepsilon$  at the left of the equation is strain hardening rate  $\theta$ . At elastic deformation and initial stage of plastic deformation, uniform elongation occurred since  $\theta$  is significantly larger than  $\sigma$ . However,  $\theta$  usually decreases monotonously during stretching, and when  $\theta = \sigma$ , necking happens and the tensile sample quickly breaks and fails. Fig. 1a schematically represents uniform elongation (necking onset) changes (dashed curves) with increasing strength of a material. The rising solid lines in the lower part of Fig. 1a present tensile true stress-strain curves, the falling solid lines in the upper part of Fig. 1a are strain hardening rate curves, and their intersection points represent necking onset points or uniform elongation. One can see that enhancing strength of a material will decrease its uniform elongation even if the  $\theta$  remains unchanged, as

<sup>\*</sup> Corresponding authors.

E-mail addresses: [xiang.chen@njust.edu.cn](mailto:xiang.chen@njust.edu.cn) (X. Chen), [yhzhao@njust.edu.cn](mailto:yhzhao@njust.edu.cn) (Y. Zhao).

<https://doi.org/10.1016/j.actamat.2023.118949>

Received 1 November 2022; Received in revised form 6 April 2023; Accepted 12 April 2023

Available online 14 April 2023

1359-6454/© 2023 Acta Materialia Inc. Published by Elsevier Ltd. All rights reserved.

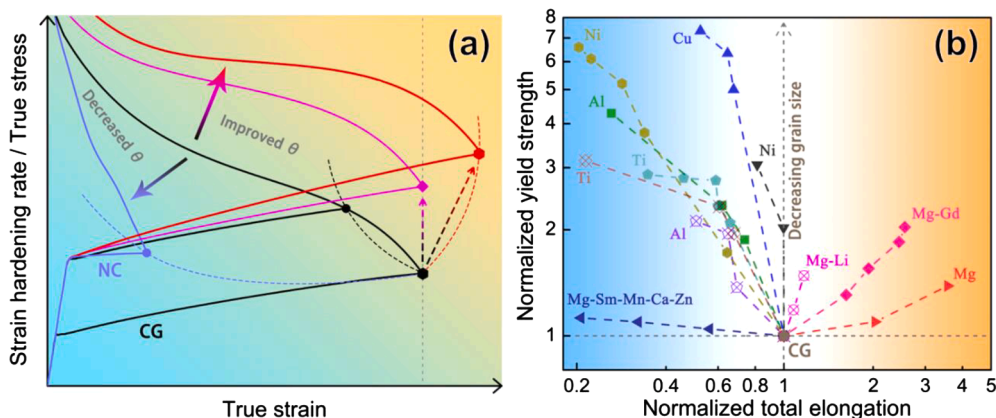


Fig. 1. (a) Schematic representation of uniform elongation (necking onset) changes (dashed curves) with increasing strength of a material. (b) Literature review of normalized yield strength versus elongation to failure of NC and CG FCC Al, Cu, Ni and HCP Ti, Mg and Mg alloys [12,22, 26–33].

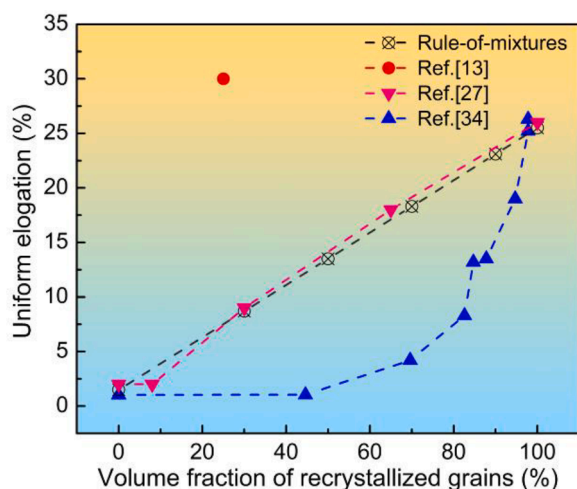


Fig. 2. Uniform elongation versus volume fraction of recrystallized grains of Cu [13,27,34].

shown by the “banana” shaped dashed black line. For the nanocrystalline (NC,  $d < 100$  nm) and ultrafine-grained (UFG,  $d < 1$   $\mu$ m) materials, unfortunately, their  $\theta$  (upper blue solid line) reduced more significantly comparing with their coarse-grained (CG) counterpart because their small grains could not accumulate or accommodate dislocations. Thus, premature necking is easy to occur even at a small tensile strain, and their tensile stress-strain curves peak quickly after yielding. As a result, the uniform elongation decreases in a much quicker “banana” curve (dashed blue curve). The intersected magenta lines show that if we want to improve the strength and still keep the uniform elongation unchanged, we must have enough additional  $\theta$ . If the extra  $\theta$  is large enough, we can even improve the uniform elongation while increasing the strength, as shown by the red dashed inverse “banana” curves. There is no doubt that this is the ideal situation we want most.

In the last twenty years, people have made great efforts to improve the poor ductility of NC and UFG metals, and many solutions have been proposed, including removing manufacturing artifacts [2,3], nanoscale precipitates/dispersions in NC and UFG metallic materials [4,5], nanotwinned grains [6,7], transformation-induced-plasticity (TRIP) and twinning-induced-plasticity (TWIP) effects [8,9], bi-/multi-modal grain size distributions [10–13], gradient structure [14–17], lamella structure [18–20], heterogeneous lamella (HL) structure [21,22], harmonic structure (HS) [23–25], etc. Although the above various strategies have achieved more or less success in improving the poor ductility of NC and UFG materials; but the enhanced ductility is still much smaller than their

CG counterparts for most of the strategies. Fig. 1b reviewed the normalized yield strength (YS) versus elongation to failure of NC and CG face-centered cubic (FCC) Al, Cu, Ni and hexagonal close-packed (HCP) Ti, Mg and Mg alloys in literature [12,22, 26–33]. It is interesting to see that the data points of all FCC metals lie in the left half of Fig. 1b, i.e. strength and ductility paradox still exists. However, for the data points of HCP metals, though some of them are still lying in the left half of Fig. 1b, some other data is distributed in the right half of Fig. 1b, i.e. strength and ductility increase simultaneously. This is undoubtedly a very important clue, and its underlying reason is worthy of in-depth study.

In Fig. 1b, metals and alloys prepared by different strategies have different varied curves of normalized YS vs normalized ductility, this means for the FCC metals, different strategies can cause different decreasing trend of ductility with increasing strength due to different microstructures. More specifically, even for bi-/multi-modal grain size distribution of Cu, different variations of uniform elongation against volume fraction of recrystallized grains are reported [13,27,34], as summarized in Fig. 2. Zhao et al. [27] found the behavior of multi-scale Cu can be predicted using the simple weighted averages of the strength and ductility of UFG and CG components, i.e., following the rule-of-mixtures. However, Wang et al. [13] and Li et al. [34] reported both positive (i.e., improved) and negative (i.e., diminished) deviations from the rule-of-mixtures, respectively. As a positive instance, Wang et al. [13] introduced 25 vol% recrystallized CGs into an UFG Cu sample, achieving a comparable total elongation (65%) compared with the CG Cu counterpart (70%) and an extraordinary uniform elongation of 30%. On the contrary, when annealing a NC Cu prepared by dynamic plastic deformation, the recovered tensile elongations were much below the rule-of-mixtures [34]. In the NC Cu, with increasing volume fraction of recrystallized grains, the ductility gradually increased along with the decreased strength, and a remarkable improvement of uniform elongation occurred only when the recrystallized CGs reached 90 vol% [34]. To reasonably explain the mechanisms of the above-described paradoxical trends, the differences in microstructure need to be considered, for instance, grain size differences and spatial distribution between the UFGs and CGs. Most importantly, the best heterogeneous grain structures (HGSS) corresponding to the positive deviations from the rule-of-mixtures should be studied clearly.

In this work, we selected HCP commercial purity (CP) Ti as the model material and bulk multi-modal CP Ti was fabricated by equal-channel-angular pressing (ECAP) process followed by subsequent annealing. Our research has two purposes, 1) to further test the possibility of simultaneously improving strength and ductility of HCP metals, and its underlying mechanisms, 2) to search the best multi-modal microstructures corresponding to the positive deviations from the rule-of-mixtures and underlying mechanisms.

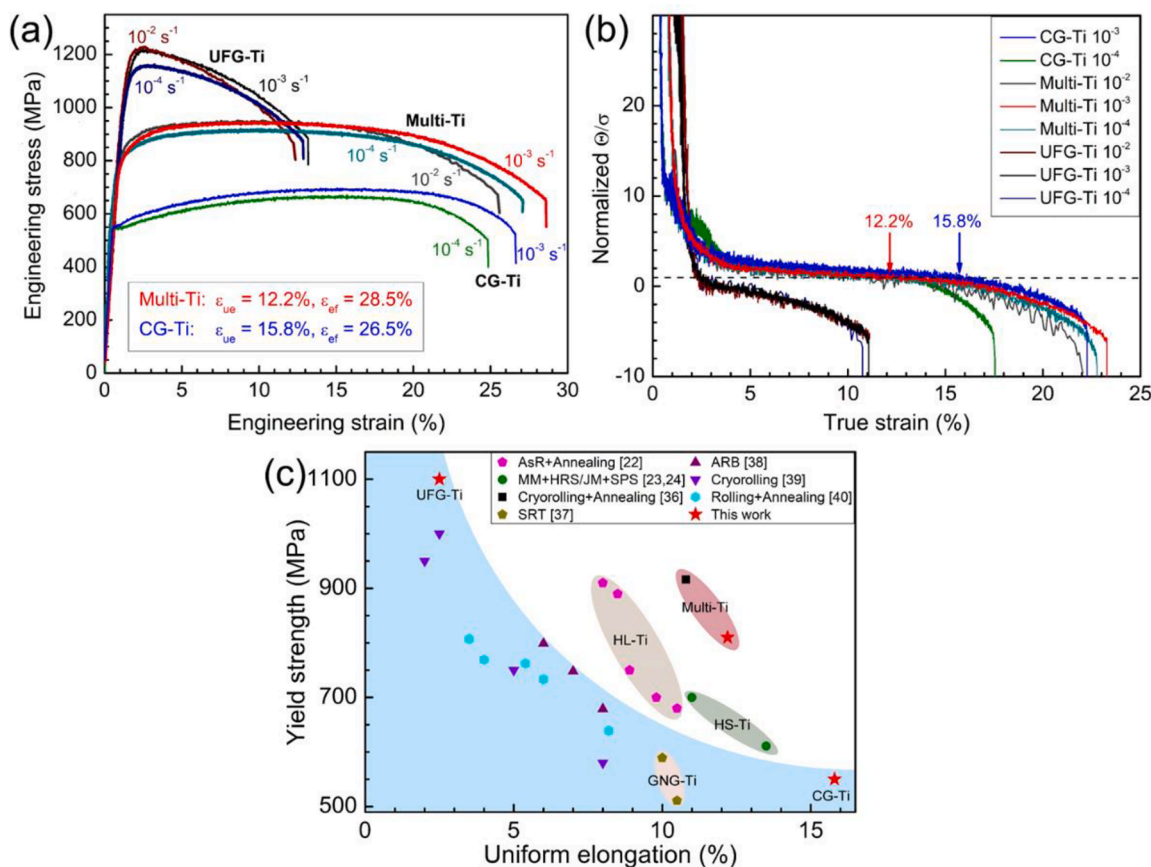


**Fig. 3.** (a) Tensile engineering stress-strain curves of UFG-, multi- and CG-Ti at different strain rates of  $10^{-4}$ – $10^{-2}$  s $^{-1}$ . (b) Normalized strain hardening rate  $\theta/\sigma$ , the true strains corresponding to the onsets of necking instability are pointed out by arrows. (c) Comparison of yield strength versus uniform elongation of our multi-Ti with literature reported data [22–24,36–40]. AsR, asymmetrical rolling; MM, mechanical milling; HRS, hot roll sintering; JM, jet milling; SPS, spark plasma sintering; SRT, surface rolling treatment; ARB, accumulative roll bonding; HL, heterogeneous lamella; HS, harmonic structure; GNG, gradient nanograin.

## 2. Experimental materials and procedures

### 2.1. Sample preparation

CP Ti, used as the starting material, has a composition (in wt.%) of 0.34% O, 0.2% Fe, 0.05% C, and 0.005% N. The billets were subjected to ECAP processing with route B<sub>C</sub> (rotating 90° in the same direction between each pass [35], as shown in Fig. S1) for 4 passes at room temperature, designated as UFG-Ti. The UFG-Ti was finally annealed at 350 °C for 6 h to form multi-modal grain size distribution, designated as multi-Ti, and annealed at 500 °C for 50 h to form CG-Ti.

### 2.2. Tensile and jump testing

Flat dog-bone-shaped tensile specimens with gage dimensions of  $1 \times 2 \times 10$  mm<sup>3</sup> were sectioned by electrical discharge machining from the central of the Ti bars with the tensile direction (TD) parallel to the ECAP extrusion direction (ED). All tensile specimens were polished before testing using a diamond suspension with particle size of 0.25 μm. The tensile tests were performed on an Instron 8801 universal testing machine using Bluehill 2 software at different strain rates. The strain was measured using a standard non-contacting video extensometer with a 100 mm field-of-view lens. Three tensile specimens were prepared for each sample to obtain results in order to ensure reproducibility. To measure strain rate sensitivity, the CG-Ti and multi-Ti tensile specimens were tested at  $10^{-3}$  s $^{-1}$  first. After yielding, the tensile strain rate was alternated among  $10^{-3}$  s $^{-1}$ ,  $10^{-4}$  s $^{-1}$  and  $10^{-5}$  s $^{-1}$ . The cyclic load-unload-reload (LUR) tensile tests were performed to measure the HDI stresses. During the LUR tensile tests, the CG-Ti and multi-Ti tensile

specimens were tensioned to an assigned strain (1%), unloaded to 50 N, and then reloaded.

### 2.3. Microstructure characterization

Microstructures from top-view (perpendicular to the TD) or side-view (parallel to the TD) of the UFG-, multi- and CG-Ti samples before and after tensile testing were characterized using X-ray diffraction (XRD), transmission electron microscopy (TEM), electron backscattered diffraction (EBSD), transmission Kikuchi diffraction (TKD) and scanning electron microscopy (SEM) measurements. First, the initial microstructures of the three samples were analyzed. Second, the gage parts of tensile specimens at tensile strains of ~2% and ~12% for multi-Ti and CG-Ti were selected for analysis of initial deformation. Third, the necking parts of the fractured tensile specimens were used to analyze the later stage of deformation.

The TEM specimens were prepared by two methods. One is the small pieces of side-view were sectioned from the tensile specimens and polished into thin foils with thicknesses of about 50 μm. Then the thin foils were twin-jet electro-polished by a solution of 25 vol% nitric acid +75 vol% Methanol for 2 min at a voltage of 15 V and a temperature of 243 K. The other is the lamellae of top-view were cut by a focus ion beam (FIB) from the polished tensile specimens. The lamellae were finally polished with 20 pA at 30 kV for TEM and TKD observations. TEM observations were carried out on a FEI TECNAI 20 electron microscopy operated at 200 kV.

The EBSD specimens were mechanically polished first and then electro-polished using an electrolyte consisting of 10 vol% perchloric acid and 90 vol% acetic acid in a Buehler electromet-4 with a voltage of

**Table 1**

Lists of yield strength (YS), ultimate tensile strength (UTS), uniform elongation  $\epsilon_{ue}$  and elongation to failure  $\epsilon_{ef}$  of the UFG-, multi- and CG-Ti.

Samples	YS (MPa)	UTS (MPa)	$\epsilon_{ue}$ %	$\epsilon_{ef}$ %
UFG-Ti	1100	1210	2.5	13
multi-Ti	800	950	12.2	28.5
CG-Ti	550	680	15.8	26.5

35 V at room temperature. EBSD, TKD and FIB measurements were performed on Carl Zeiss Auriga focused ion beam scanning electron microscope equipped with an Oxford Instruments Aztec system (channel 5 software). The operating voltages were set to 20 kV for EBSD and 30 kV for TKD. EBSD data from side-view and TKD data from top-view were analyzed for crystal orientation, grain size and grain boundary (GB) misorientation angle distribution, recrystallization and local misorientation. Boundaries with misorientation angles  $>2^\circ$  were considered as low-angle GBs (LAGBs,  $2-15^\circ$ ) and high-angle GBs (HAGBs,  $>15^\circ$ ). The  $\{0001\}$  and  $\{10\bar{1}0\}$  pole figures for texture analysis were obtained from microscopic EBSD and macroscopic XRD data, respectively. The high-resolution XRD measurements were performed on PANalytical X-ray diffractometer (XPert MRD) with Cu-K $\alpha$  radiation using 40 mA at 40 kV. The fracture surfaces and morphologies were imaged by a FEI-XL30 SFESEM using a 25 kV beam.

### 3. Results

#### 3.1. Mechanical properties

The representative engineering stress-strain curves of the UFG-, multi- and CG-Ti samples at different strain rates are compared in Fig. 3a. The effect of strain rate on the tensile behavior were unobvious and the optimal strength and ductility combination were obtained at the tensile strain rate of  $10^{-3} \text{ s}^{-1}$  for all three samples. First, the CG-Ti has a YS of 550 MPa, an ultimate tensile strength (UTS) of 680 MPa and a uniform elongation of 15.8%, a fracture elongation of 26.5%, as listed in Table 1. Then ECAP processing elevates the YS up to 1100 MPa but leads to the reduction of the uniform elongation down to 2.5%. After annealing at 350 °C for 6 h, the strain hardening capacity is enhanced and the uniform elongation increases substantially. The multi-Ti has a high YS of 800 MPa and an excellent fracture elongation of 28.5%. The uniform elongation of the multi-Ti is 12.2%, close to the CG-Ti (15.8%). There exists an extra larger strain hardening causing the tensile curve keeps going up in the multi-Ti sample. Fig. 3b illustrates the strain hardening rate drops at first for all three samples. When the true strain is larger than 2.5%, the normalized  $\theta/\sigma$  of the UFG-Ti is smaller than 1 and drops fastest, exhibiting lowest strain hardening rate. Notably, the

multi-Ti and CG-Ti have the same varying tendency and show slow drop of the normalized  $\theta/\sigma$  with increasing strain.

Fig. 3c compares the YS versus uniform elongation of our multi-Ti with literature data, including various Ti samples by different processing methods [22–24,36–40]. A number of HGS Ti containing HL-Ti (heterogeneous lamella Ti) [22], HS-Ti (harmonic structure Ti) [23, 24] and multi-Ti [36], have the superior combination of YS and uniform elongation. In contrast, multi-Ti has the higher YS compared to HL-Ti and a better uniform elongation compared to HS-Ti.

Based on Hart's theory [41], tension necking instability can be described as:

$$\frac{\theta}{\sigma} \leq 1 - m \quad (2)$$

where  $m$  is the strain rate sensitivity, reflects thermally activated mechanisms of slip and contributes to plastic deformation processes in metals.  $m$  can be written as:

$$m = \left( \frac{\partial \ln \sigma}{\partial \ln \dot{\epsilon}_p} \right)_{\epsilon} \quad (3)$$

where  $\dot{\epsilon}_p$  is the true strain rate. Fig. 4a shows true stress-strain curves of the multi- and CG-Ti by strain rate jump test at  $10^{-2}$ ,  $10^{-3}$  and  $10^{-4} \text{ s}^{-1}$ , and Fig. 4b shows the calculated  $m$  which are averagely 0.022 for the CG-Ti sample and 0.019 for the multi-Ti sample. Note that  $m$  of CP Ti consisting of UFGs is averagely 0.013 in the literature [42].  $\theta$  is mainly resulted from dislocation multiplication and interactions between dislocation and other lattice defects as well as itself. Both high  $\theta$  and  $m$  are important for high tensile ductility, aiding with delaying the necking and prolonging the elongation.

#### 3.2. Initial microstructures before tensile tests

The elongated deformed grains with high-density dislocations were introduced by ECAP in the UFG-Ti sample (Fig. 5a). The grains are parallel to the ED of ECAP and most GBs are wavy and obscure. The transverse grain size of the UFG-Ti sample is 224 nm in average. From the EBSD mapping in Fig. 6a, the sample contains numerous elongated grains including sub-grains, and ultrafine equiaxed grains. The equiaxed grains were most likely formed during ECAP by dynamic recrystallization due to deformation heat. From the GB misorientation angle distribution shown in Fig. 6g, the UFG-Ti has  $\sim 56\%$  HAGBs and  $\sim 44\%$  LAGBs. No distinct twin boundaries are captured, such as common  $\sim 65^\circ$  and  $\sim 85^\circ$  corresponding to  $\{11\bar{2}2\}$  compression twins and  $\{10\bar{1}2\}$  extension twins [43,44], can be seen in the UFG-Ti, indicating deformation twins were not captured after 4 passes ECAP processing. Earlier studies have shown that the deformation mechanism changed from

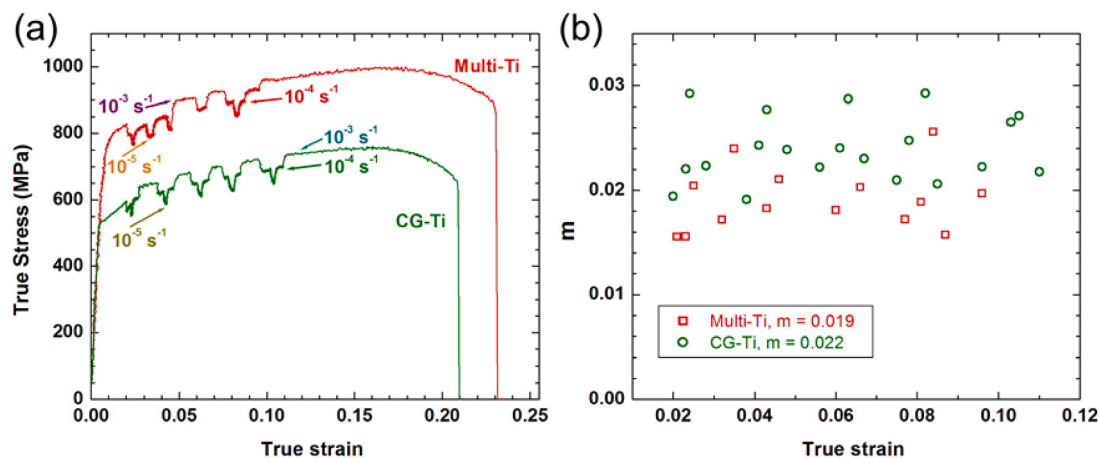


Fig. 4. (a) Jump test curves of the multi- and CG-Ti specimens. (b) Strain rate sensitivity  $m$  against true strain of the multi-Ti and CG-Ti samples.

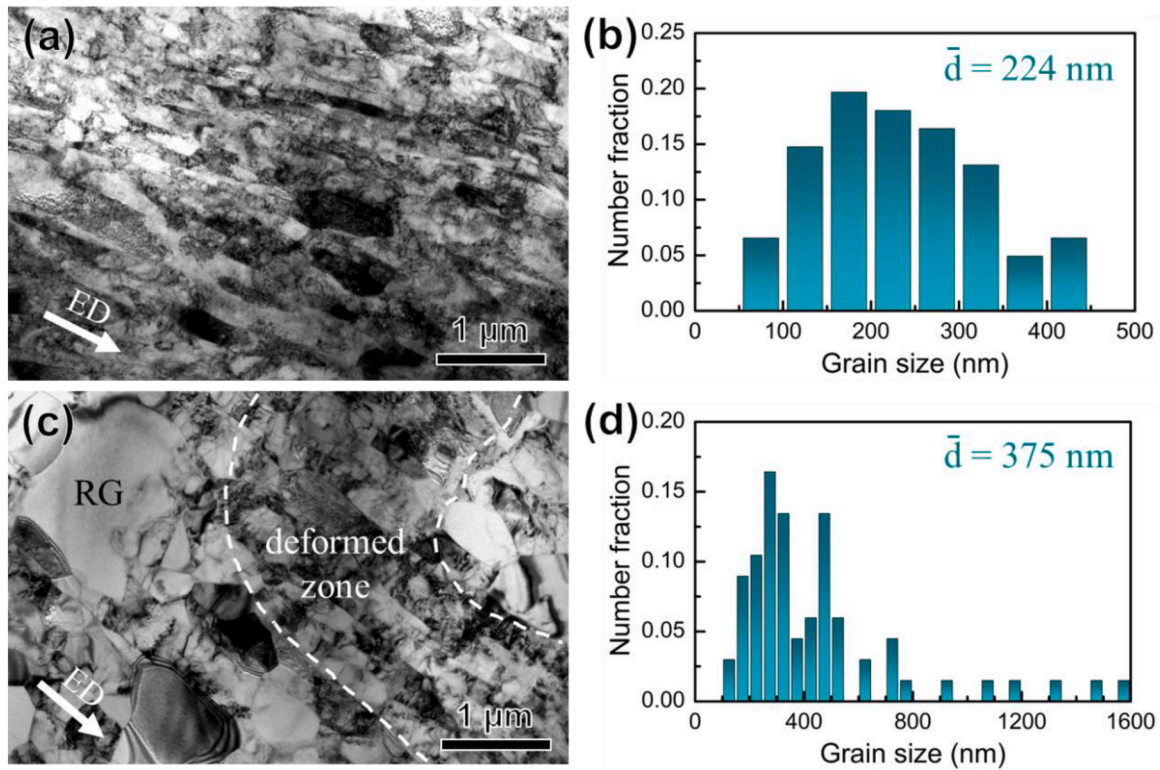


Fig. 5. Bright-field TEM images from side-view and corresponding grain size distribution of the initial UFG-Ti (a, b) and multi-Ti samples (c, d).  $\bar{d}$ , average grain size; ED, extrusion direction; RG, recrystallized grain.

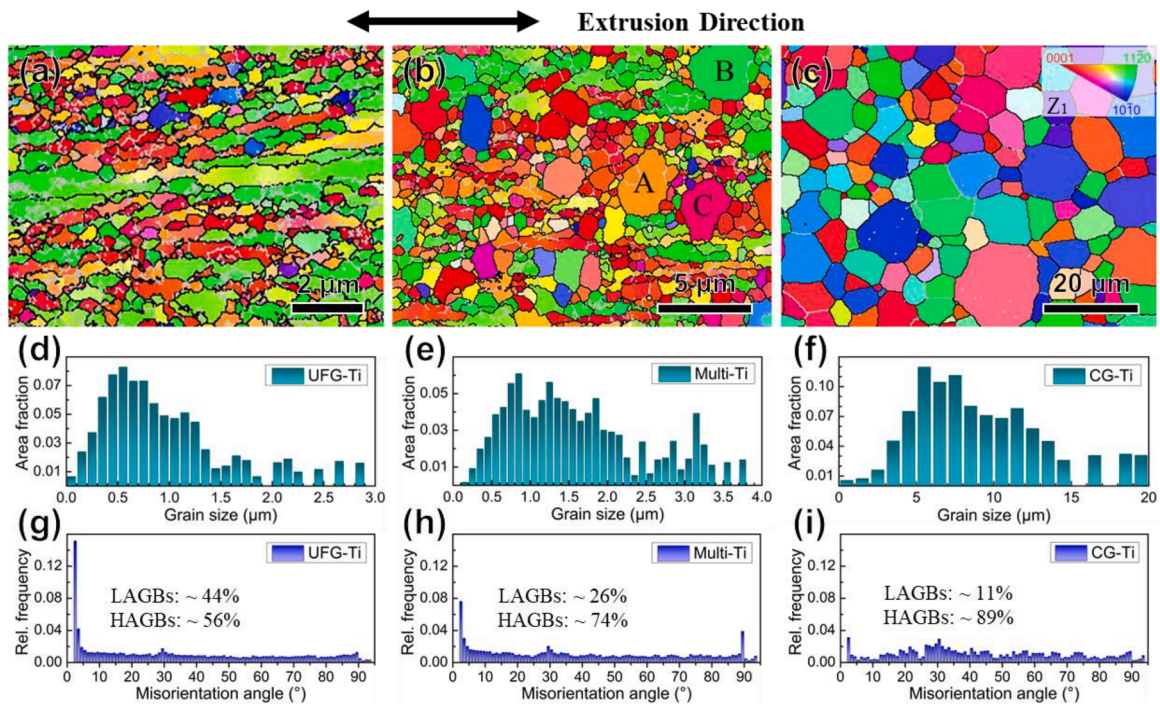
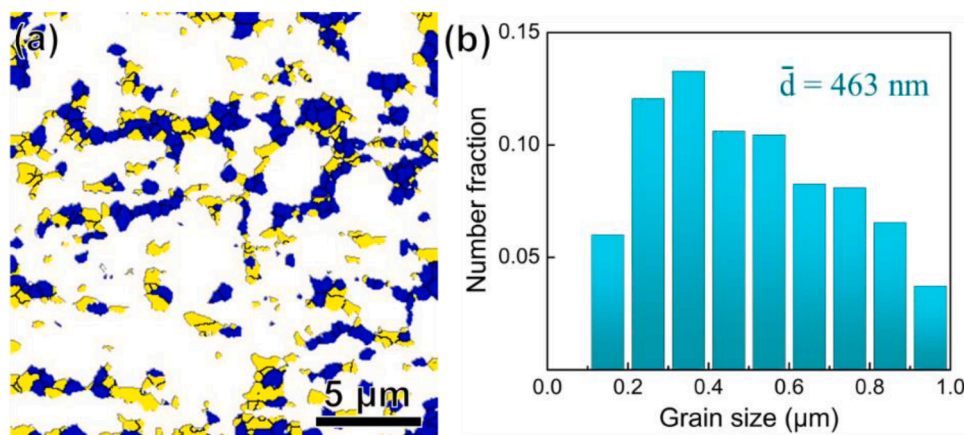


Fig. 6. EBSD crystal orientation maps from side-view, distributions of grain size and grain boundary (GB) misorientation angle of (a, d, g) UFG-Ti, (b, e, h) multi-Ti and (c, f, i) CG-Ti samples. The color code is inserted in (c). The low- and high-angle GBs are marked by gray and black lines, respectively. IPF color of Z1 perpendicular to extrusion direction (ED) is applied.

twinning to dislocation slip in CP Ti after the second pass of ECAP [45]. The deformation twins were formed at the early stage and then evolved into the grain boundaries, serving as the grain refinement mechanism

[45,46]. Further analyses in the Ref. [45] revealed that grain refinement and texture formation during the first pass increased the critical resolved shear stress for twinning. The EBSD and XRD measured pole figures



**Fig. 7.** The recrystallization map (a) and corresponding grain size distribution (b) of the submicron-sized grains in the multi-Ti sample. Blue and yellow represent recrystallized and deformed grains, respectively. The black lines in (a) are HAGBs.

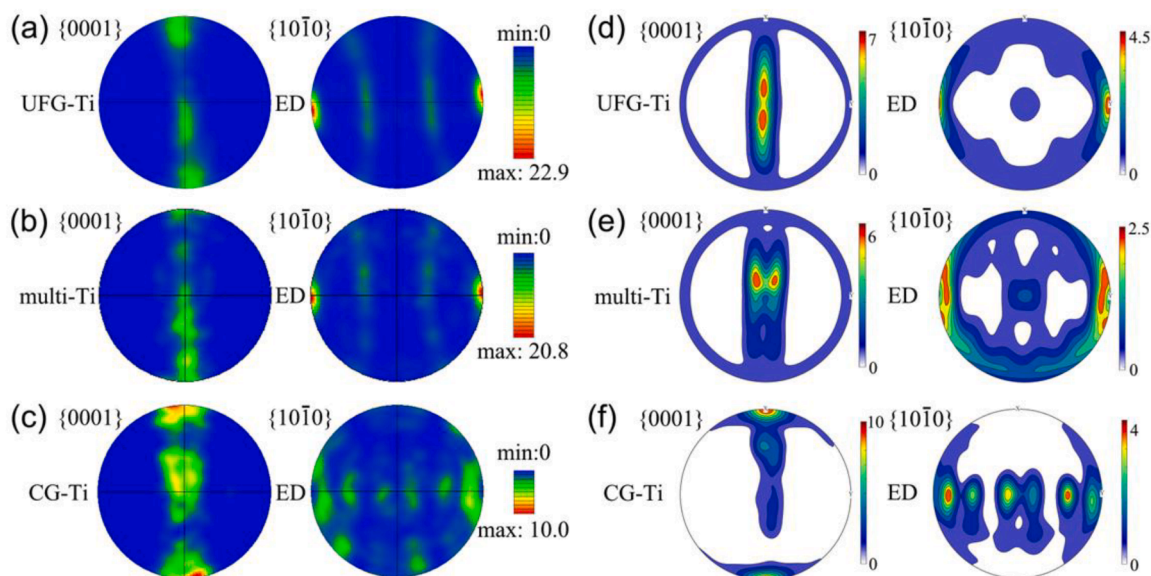


**Fig. 8.** EBSD (a-c) and XRD (d-f) measured  $\{0001\}$  and  $\{10\bar{1}0\}$  pole figures of the initial (a, d) UFG-Ti, (b, e) multi-Ti and (c, f) CG-Ti samples. ED, extrusion direction.

show the maximum intensity of  $\{10\bar{1}0\}$  plane is almost perpendicular to ED of the UFG-Ti (Fig. 8a,d). The grain size distribution is estimated to be 393 nm via EBSD, larger than the TEM data (224 nm). This is due to the limitation of the scanning step size (50 nm), unable to resolve some grains smaller than 100 nm.

After annealing, the multi-Ti is partially recrystallized and consists of a mixed microstructure containing recrystallization and deformation (dashed area in Fig. 5c) zones. The recrystallization zone is composed of micron- and submicron-sized equiaxed grains, of which GBs are discernable. The noteworthy feature is that the individual micron-sized recrystallized grains are surrounded by a string of UFGs, further verified by EBSD (see grains A-C in Fig. 6b). Most UFGs in the recrystallization zone have a very low dislocation density. On the contrast, the UFGs in the deformation zone have higher dislocation densities, but lower than the UFG-Ti sample (Fig. 5a). The average grain size increases to 375 nm for the multi-Ti, which shows a multi-modal distribution (Fig. 5d). From EBSD analysis, the multi-Ti has a wide grain size distribution from 100 nm to 3.8  $\mu\text{m}$  and an average grain size of 725 nm (Fig. 6b). The multi-Ti consists of 30 vol% micron-sized recrystallized grains, 60 vol% submicron-sized equiaxed grains, 10 vol% elongated deformed grains. The submicron-sized grains are made of half recrystallized grains and

**Table 2**

The Schmid factors of four slip systems for the UFG-Ti, multi-Ti and CG-Ti samples before tensile deformation.

Samples	$\{0001\}$ $\langle 11\bar{2}0 \rangle$	$\{10\bar{1}0\}$ $\langle 11\bar{2}0 \rangle$	$\{10\bar{1}1\}$ $\langle 11\bar{2}0 \rangle$	$\{10\bar{1}1\}$ $\langle 11\bar{2}3 \rangle$
UFG-Ti	0.086	<b>0.454</b>	0.378	<b>0.469</b>
multi-Ti	0.099	<b>0.456</b>	0.389	<b>0.461</b>
CG-Ti	0.137	<b>0.467</b>	0.410	<b>0.461</b>

half deformed grains with an average grain size of 463 nm (Fig. 7). The fraction of HAGBs in the multi-Ti increases to 74% (Fig. 6h). Both XRD and EBSD pole figure shows the texture of the multi-Ti did not changed upon annealing and only the intensity of  $\{10\bar{1}0\}$  plane slightly decreased (Fig. 8b,e). As shown in Fig. 6c, complete recrystallization with an average grain size of  $\sim 5.7 \mu\text{m}$  occurs in the CG-Ti after annealing. The fraction of HAGBs increases to 89% (Fig. 6i). The preferred orientation of the CG-Ti turned into the maximum intensity of  $\{0001\}$  plane (Fig. 8c,f). The average Schmid factors of different slip systems for these three samples are calculated, as shown in Table 2. It can be found all three samples have similar Schmid factors of  $\{10\bar{1}0\}$

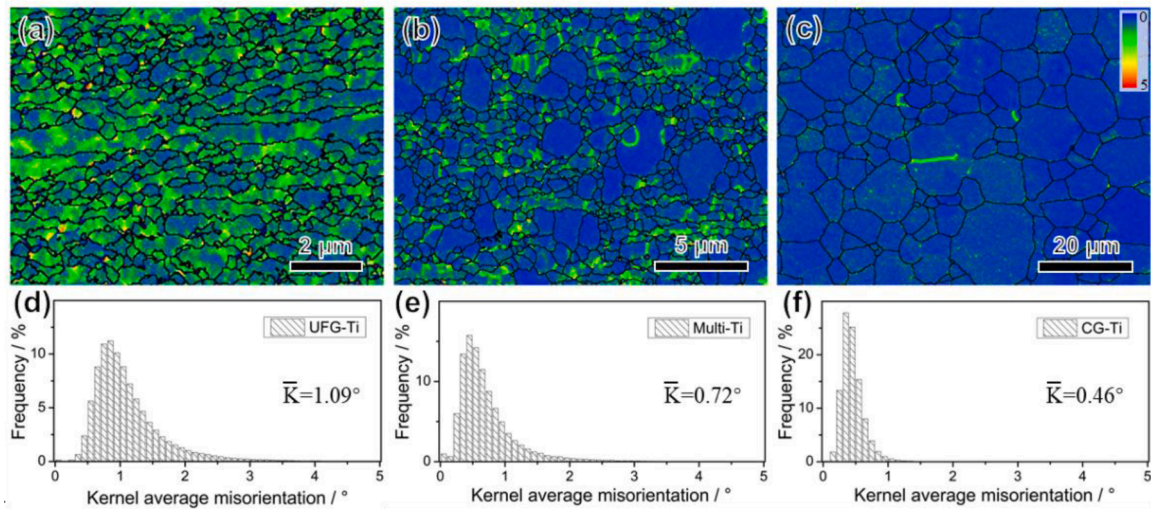


**Fig. 9.** Local misorientation maps from side-view and corresponding Kernel average misorientation (KAM) value distributions of (a, d) UFG-Ti, (b, e) multi-Ti and (c, f) CG-Ti samples. The inset in (c) is the rainbow color bar (blue to red represent small to large misorientation). The black lines in (a-c) are HAGBs.  $\bar{K}$ : average KAM value.

**Table 3**

Lists of HAGBs fraction ( $F_{\text{HAGBs}}$ ), the volume fraction of coarse-grains ( $F_{\text{CGs}}$ ) and ultrafine-grains ( $F_{\text{UFGs}}$ ), average grain size ( $\bar{d}$ ) and the density of GNDs ( $\rho$ ) of the UFG-, multi- and CG-Ti samples from EBSD data.

Samples	$F_{\text{HAGBs}}$ (%)	$F_{\text{UFGs}}$ (%)	$F_{\text{CGs}}$ (%)	$\bar{d}$ ( $\mu\text{m}$ )	$\rho$ ( $\text{m}^{-2}$ )
UFG-Ti	56	100	–	0.393	$1.28 \times 10^{15}$
Multi-Ti	74	70	30	0.725	$8.5 \times 10^{14}$
CG-Ti	89	–	100	5.7	$2.7 \times 10^{14}$

$\langle 11\bar{2}0 \rangle$  and  $\{10\bar{1}1\} \langle 11\bar{2}3 \rangle$  slip systems. Therefore, the influence of texture on mechanical properties is weak for these samples.

The average Kernel average misorientation (KAM) value of the UFG-Ti is  $1.09^\circ$  and then decreases to  $0.72^\circ$  for the multi-Ti and  $0.46^\circ$  for CG-Ti after annealing (Fig. 9). The geometrically necessary dislocations (GNDs) density was related to the average KAM value according to Kubin [47] and Gao [48]:

$$\rho = \frac{\theta^{\text{KAM}}}{ub} \quad (4)$$

where  $\rho$  is the GNDs density;  $u$  is the step size, used in EBSD acquisition;  $b$  is the length of the Burgers vector ( $1/3 \langle 11\bar{2}0 \rangle$  was used to calculate,  $0.295 \text{ nm}$  for Ti [42]);  $\theta^{\text{KAM}}$  is the average KAM value. The calculated GNDs densities are  $1.28 \times 10^{15} \text{ m}^{-2}$  for the UFG-Ti,  $8.5 \times 10^{14} \text{ m}^{-2}$  for the multi-Ti and  $2.7 \times 10^{14} \text{ m}^{-2}$  for the CG-Ti, as listed in Table 3.

### 3.3. Microstructural evolutions under tension

Microstructural evolutions of the multi-Ti and CG-Ti samples during tensile testing were performed by EBSD, TEM, TKD and SEM. Specifically, deformation mechanisms at low strain stage (at the engineering strains of  $\sim 2\%$ ,  $\sim 12\%$ ) and high strain stage (at necking) were analyzed.

#### 3.3.1. Grain size and grain boundaries

Microstructure evolutions for the multi-Ti and CG-Ti with comparable ductility were compared during tensile loading in Figs. 10 and 11. Firstly, the grain spatial distribution from side-view (Fig. 10a,c) and top-view (Fig. 11) further demonstrates the multi-Ti consists of  $\sim 30 \text{ vol}\%$  micro-grains surrounded by the UFGs in three dimensions. The color variations in the grain interior indicate the large changes of

misorientation caused by pronounced dislocation accumulation. With the increasing strains to necking, the average grain size of the multi-Ti slightly decreases from  $725 \text{ nm}$  to  $647 \text{ nm}$  and then to  $625 \text{ nm}$  (Fig. 10e). The volume fraction of LAGBs increases from  $26\%$  to  $33\%$  and then to  $52\%$  (Fig. 10g). Secondly, a large number of LAGBs (gray lines) are introduced in the homogeneous CG-Ti under tension (Fig. 10b,d). The volume fraction of LAGBs increases rapidly from  $11\%$  to  $68\%$  and then to  $82\%$  (Fig. 10g), due to the pronounced accumulation and arrangement of dislocations (mainly GNDs). The average grain size of the CG-Ti decreases from  $5.7 \mu\text{m}$  to  $2.8 \mu\text{m}$  and then to  $2.3 \mu\text{m}$  (Fig. 10f). Fig. 10e shows the consistent multi-modal grain size distribution in the deformed multi-Ti. At the same uniform strain of  $\sim 12\%$ , the multi-Ti has lower density of LAGBs with  $33\%$  compared with the CG-Ti ( $68\%$ ). At necking, the CG-Ti also has higher LAGBs density. It indicates that the multiplication, accumulation and entanglement of dislocations occur dramatically and more dislocation substructures are produced in the CG-Ti during tensile plastic deformation.

#### 3.3.2. Dislocation and strain distribution

The local misorientation maps of the multi-Ti and CG-Ti samples at different tensile strains are shown in Fig. 12. The rainbow color bar from blue to red inset in Fig. 12b represents small to large local misorientation. The KAM method was used to determine the local misorientation based on the EBSD data [49]. The threshold value of local misorientation was defined as  $5^\circ$ . The filter size with  $5 \times 5$  was used to produce a smooth misorientation map. After  $\sim 12\%$  tension, the multi-Ti shows blue color in many areas, containing all the micro-grains interiors and the fractional UFGs interiors, which have lower density of GNDs (Fig. 12a). The color changes from GBs with green to interiors with blue in multi-Ti, indicative of the existence of strain gradient. However, the CG-Ti nearly shows green in the whole map and the minority maintain blue color inside of grains under the same strain (Fig. 12b), indicating all grains deformed together and stored high-density GNDs. At necking, the multi-Ti shows green color in all UFGs (Fig. 12c), indicating the recrystallized UFGs underwent large plastic deformation at high strain stage and accumulated high-density GNDs. For the CG-Ti, overall green covered and even partial regions are red (Fig. 12d), indicating the CG-Ti stored higher density of GNDs, which evenly distributed in all grains. The KAM value distributions of both samples after tension are shown in Fig. 12e,f. Obviously, the averaged KAM ( $\bar{K}$ ) values increase with the enhance tensile strain. The  $\bar{K}$  increases from  $0.46^\circ$  to  $1.94^\circ$  and then to  $2.29^\circ$  in the CG-Ti. For the multi-Ti, the  $\bar{K}$  increases from  $0.72^\circ$  to  $0.94^\circ$ ,

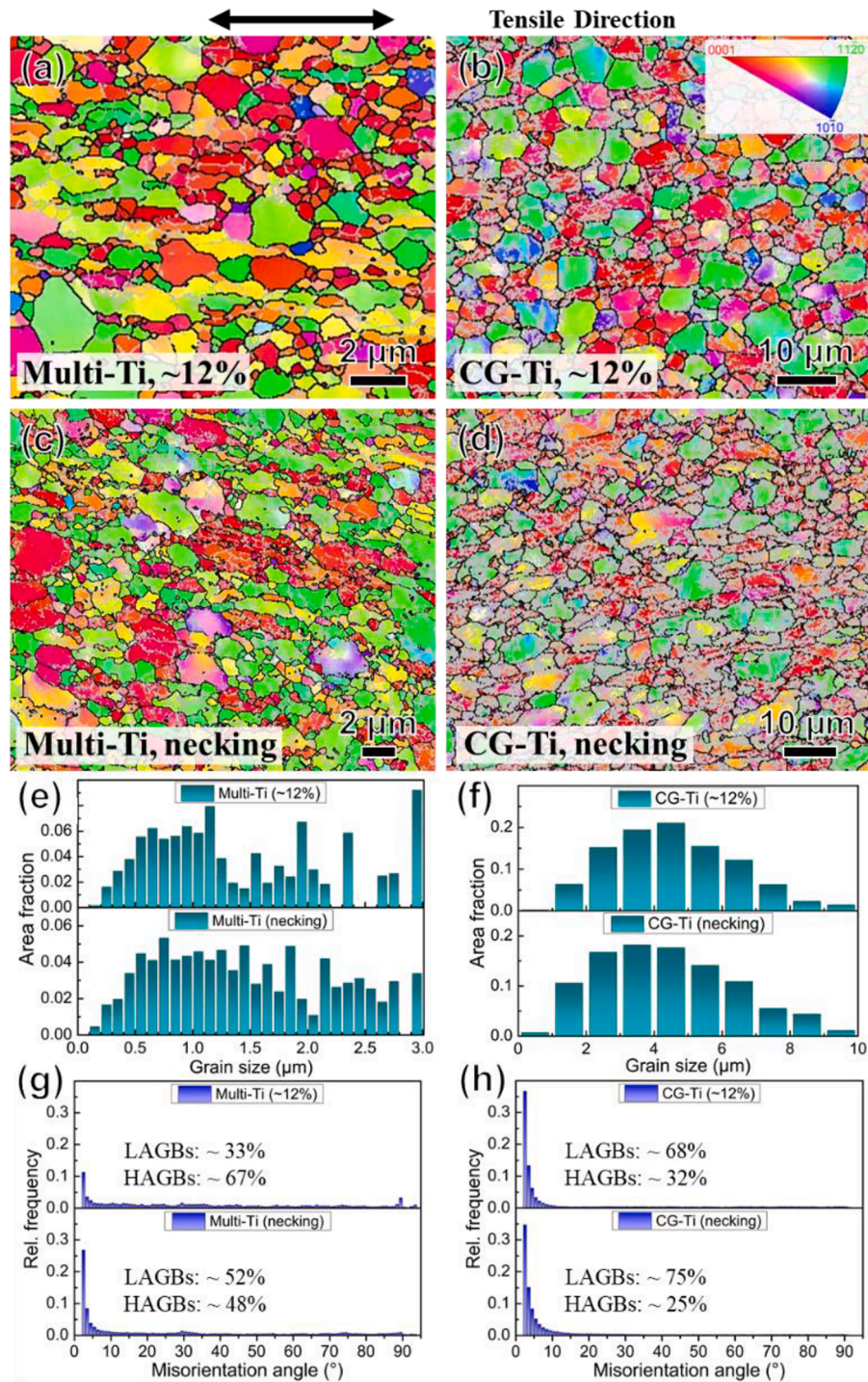


**Fig. 10.** EBSD crystal orientation maps from side-view of (a, c) multi-Ti and (b, d) CG-Ti samples at (a, b) the engineering strain of ~12% and (c, d) necking. The color code is inserted in (b). The LAGBs and HAGBs are marked by gray and black lines, respectively. The distributions of grain size and GB misorientation angle of (e, g) multi-Ti and (f, h) CG-Ti samples at different tensile strains.

and then to  $1.43^\circ$ . As mentioned before, the  $\bar{K}$  has linear relation with the density of GNDs, which can be calculated by the formula ((4)). The calculated GNDs densities are  $1.1 \times 10^{15} \text{ m}^{-2}$  and  $1.6 \times 10^{15} \text{ m}^{-2}$  for the multi-Ti,  $2.3 \times 10^{15} \text{ m}^{-2}$  and  $2.7 \times 10^{15} \text{ m}^{-2}$  for the CG-Ti after ~12% tension and at necking, respectively, as listed in Table 4.

Dislocation structures were further characterized by two-beam conditions by TEM according to the invisibility criterion of  $\mathbf{g} \cdot \mathbf{b} = 0$ , where  $\mathbf{g}$  and  $\mathbf{b}$  represent the reflection and Burgers vector, respectively [29, 50]. If  $\mathbf{g} = 0\bar{1}10$  is set,  $\langle a \rangle$  dislocations with  $\mathbf{b} = 1/3 \langle 11\bar{2}0 \rangle$  are visible,

but  $\langle c \rangle$  dislocations with  $\mathbf{b} = \langle 0001 \rangle$  are invisible. Conversely, if  $\mathbf{g} = 0002$  is set,  $\langle a \rangle$  dislocations are invisible but  $\langle c \rangle$  dislocations are visible. Additionally,  $\langle c + a \rangle$  dislocations with  $\mathbf{b} = 1/3 \langle 11\bar{2}3 \rangle$  are visible in both two-beam conditions mentioned above. Therefore, the dislocation type can be determined by using different two-beam conditions. Comparing the images under different two-beam conditions, plenty of GNDs pile-ups are located in the micro-grains at ~2% strain in the multi-Ti (Fig. 13a,c), and these dislocation arrays are invisible in the two-beam of  $\mathbf{g} = 0002$  (Fig. 13b,d), indicating these GNDs pile-ups are  $\langle a \rangle$

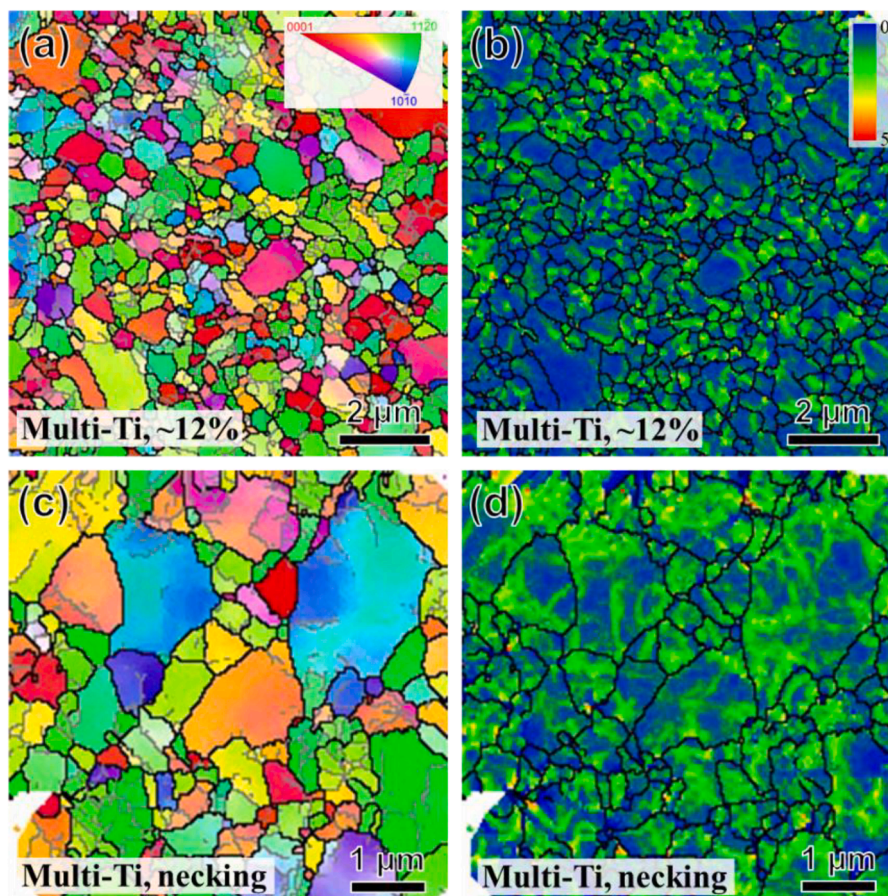


**Fig. 11.** TKD crystal orientation (a, c) and local misorientation (b, d) maps from top-view of the multi-Ti (a, b) at the engineering strain of  $\sim 12\%$  and (c, d) necking.

dislocations. In the  $\alpha$ -Ti,  $\langle a \rangle$  dislocation slip in  $\{10\bar{1}0\}$  prismatic planes is the easiest mode, because the critical resolved shear stress (CRSS) for prismatic slip is relatively low at room temperature [51,52]. Apart from  $\langle a \rangle$  dislocations, pyramidal  $\langle c + a \rangle$  dislocations are also activated (Fig. 13d). Although the CRSS for pyramidal slip is much higher in the  $\alpha$ -Ti [52], the micro-grains restrained by 3D UFGs induce stress concentration, which may contribute to the activation of  $\langle c + a \rangle$  dislocations.

TEM images of the multi-Ti at the engineering strain of  $\sim 12\%$  and necking are shown in Fig. 14a,b, respectively. A large number of GNDs pile-ups are distributed in the micro-grains (E, D), surrounded by a series of UFGs (Fig. 14a). No dislocation substructures are found in the micro-grains. For the UFGs, most have high-density tangled dislocations. Dislocation walls form in the micro-grains at necking (Fig. 14b). Furthermore, GNDs pile-ups are also found in the UFG, such as grain K in the enlarged region. From Fig. 14c,d, high-density  $\langle c + a \rangle$  dislocations as well as  $\langle c \rangle$  dislocations are formed in the micro-grains when necking. These non-basal  $\langle c \rangle$  dislocations may be formed by the dissociation of pyramidal  $\langle c + a \rangle$  dislocations [53]. For the CG-Ti at the engineering strain of  $\sim 15\%$ , very few  $\langle c + a \rangle$  dislocations were observed in the regions near the GBs and  $\langle a \rangle$  dislocation slip is the dominating deformation mechanism (Fig. 15).

### 3.4. Fracture mechanisms

To further understand the fracture behavior, SEM observations were performed on the fracture morphologies of the UFG-Ti, multi-Ti and CG-Ti, as shown in Fig. 16. All three samples fracture via ductile mechanisms, as verified by the homogeneously distributed honeycomb-like dimples over the entire fracture surface. For the UFG-Ti, most dimples

are sub-micrometer-sized and a few are larger than three micrometers. The multi-Ti has the similar dimple sizes and distribution, but it should be noted that the micron-sized dimples are deeper and larger compared to the UFG-Ti. The dimple sizes of the CG-Ti are larger than one micrometer. The corresponding dimple size distributions are counted in Fig. S2. There are cavities and micro-cracks in the fractured UFG-Ti (Fig. 16d), but only micro-cracks in the fractured multi-Ti (Fig. 16e). The fractured multi-Ti shows ridge-like feature from side-view. The enlarged view shows the micron-sized and sub-micrometer-sized ridge-like regions, due to severe strain partitioning during plastic deformation. These micron-sized "ridges" correspond to the elongated micro-grains at necking, as shown in Fig. 10c, and the sub-micrometer-sized "ridges" are the deformed UFGs during tension. For the fractured CG-Ti, a large number of slip bands are formed inside the grains, pointed by blue arrows in Fig. 16f. Moreover, the discontinuous micro shear bands pointed by yellow arrows are also uniformly distributed. The distances between micro shear bands vary from several to tens of micrometers, and the lengths range from several to one hundred micrometers.

### 3.5. HDI stress measurement

To reveal the contribution of HDI stress on the excellent strain hardening, the LUR tensile tests were performed. Fig. 17a shows the true LUR stress-strain curves of the multi-Ti and CG-Ti samples obtained. The hysteresis loops indicate the existence of uneven deformation in both samples (Fig. 17b). Due to the existence of GBs with different orientations, the inhomogeneous plastic deformation exists in the CG-Ti. The HDI stress ( $\sigma_{HDI}$ ) at different strains can be calculated by the following equation [54,55]:

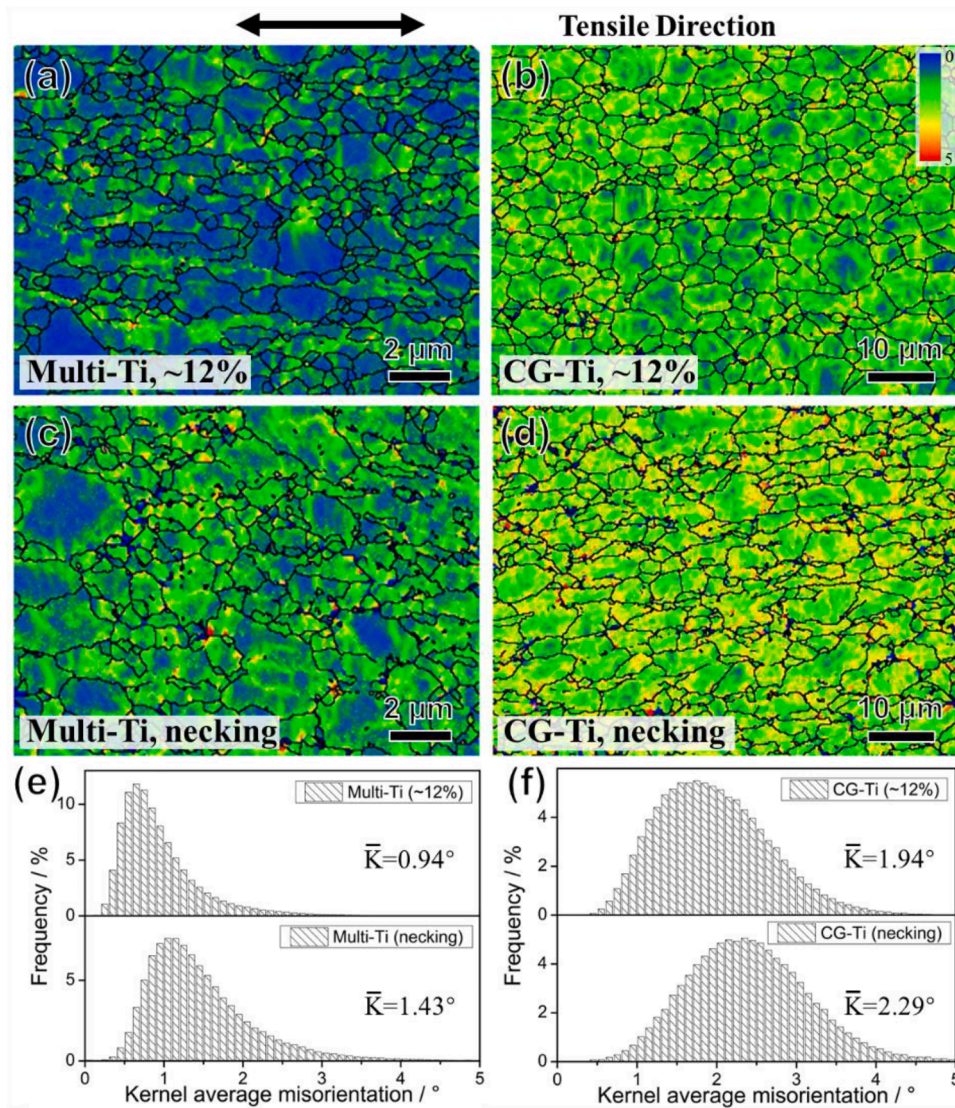


**Fig. 12.** The local misorientation maps from side-view of (a, c) multi-Ti, (b, d) CG-Ti samples at (a, b) the engineering strain of  $\sim 12\%$  and (c, d) necking. (e, f) The corresponding KAM value distributions of both samples. The inset in (b) is the rainbow color bar (blue to red represent small to large misorientation). The black lines in (a-d) are HAGBs.

**Table 4**

The evolution of LAGBs fraction ( $F_{LAGBs}$ ), average grain size ( $\bar{d}$ ) and the density of GNDs ( $\rho$ ) of the multi-Ti and CG-Ti samples under tension from EBSD data.

Samples	Multi-Ti ( $\sim 12\%$ )	CG-Ti ( $\sim 12\%$ )	Multi-Ti (necking)	CG-Ti (necking)
$F_{LAGBs}$ (%)	33	68	52	82
$\bar{d}$ ( $\mu\text{m}$ )	0.647	2.8	0.625	2.3
$\rho$ ( $\text{m}^{-2}$ )	$1.1 \times 10^{15}$	$2.3 \times 10^{15}$	$1.6 \times 10^{15}$	$2.7 \times 10^{15}$

$$\sigma_{HDI} = \frac{\sigma_r + \sigma_u}{2} \quad (5)$$

where the  $\sigma_r$  and  $\sigma_u$  are the reloading and unloading yield stress, measured from each hysteresis loop (Fig. 17b). The calculated HDI stresses increase slightly from 329 MPa to 353 MPa in the CG-Ti, but increase dramatically from 463 MPa to 582 MPa in the multi-Ti.

## 4. Discussion

Our above results confirm the possibility of simultaneously improving strength and ductility of HCP metals (Fig. 3a), and the underlying mechanisms are the actuation of additional  $\langle c + a \rangle$  slip systems of HCP metals induced by HDI hardening effect. This might be the basic reason why the data points of all FCC metals only lie in the left half of Fig. 1b, while some data points of HCP metals can locate in the right half of Fig. 1b. The lack of additional new slip system in FCC metals will reduce the HDI hardening effect. Moreover, our results also revealed the best multi-modal microstructures corresponding to the positive deviations from the rule-of-mixtures, i.e. maximum interface density between hard and soft domains, and underlying mechanisms are the maximum interface density can produce the maximum HDI hardening effect.

### 4.1. Construction of multi-modal grain structure

The micro-grains constrained by three-dimensional UFGs are carefully constructed in the multi-Ti sample. The ECAP processing induces UFGs with high stored strain energy, wherein the elongated grains

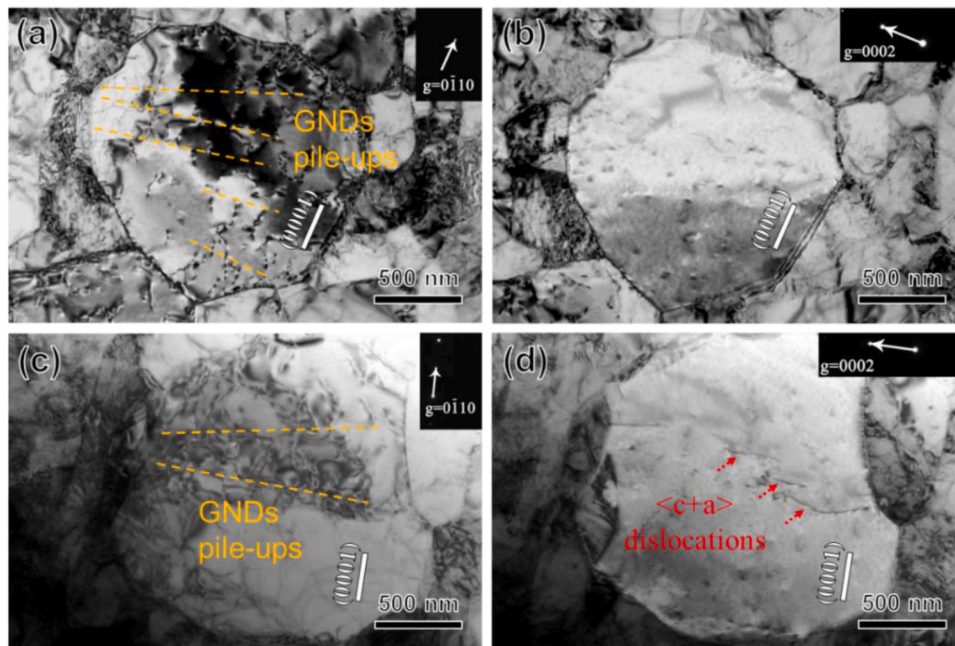


Fig. 13. TEM images in two-beam condition near the  $[2\bar{1}\bar{1}0]$  zone axis of the multi-Ti at  $\sim 2\%$  strain. Dislocation configurations in the deformed micro-grains were viewed with  $g = 0\bar{1}10$  and  $g = 0002$ , respectively. The white straight lines highlight the trace of (0001) basal plane.

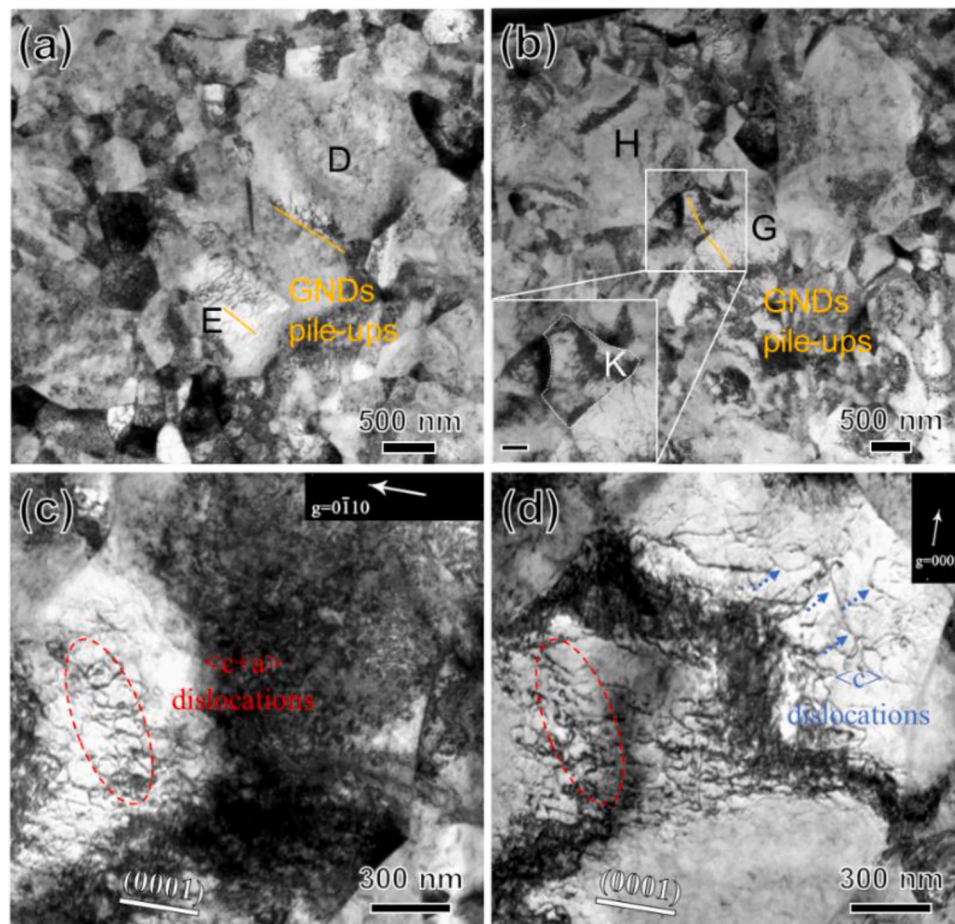
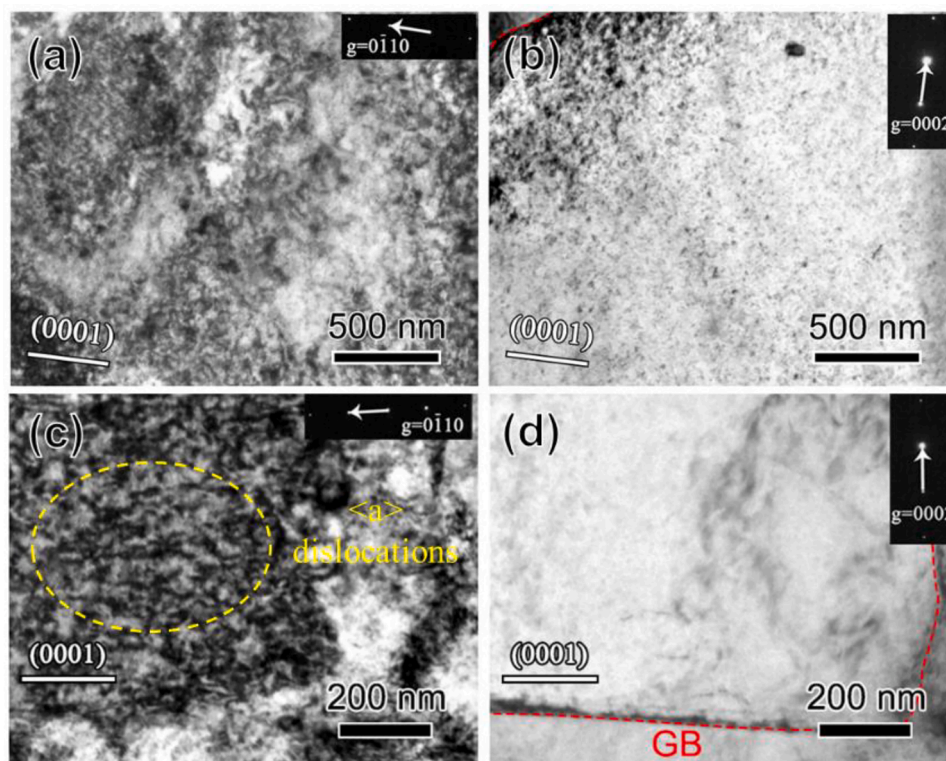
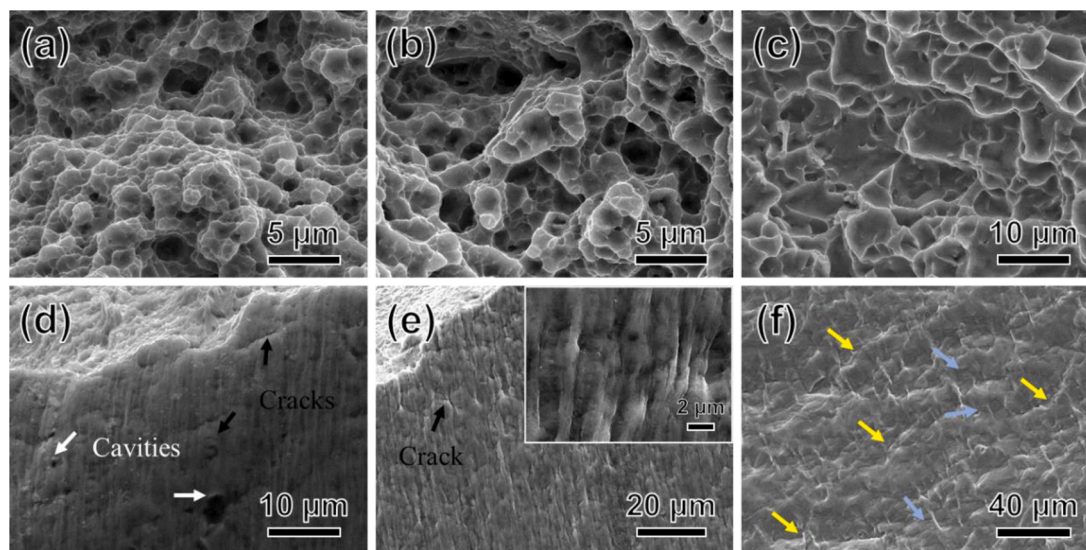


Fig. 14. TEM images from top-view of the multi-Ti at (a) the engineering strain of  $\sim 12\%$  and (b) necking. The scale bar in the enlarged region of (b) is 200 nm. Two-beam condition near the  $[2\bar{1}\bar{1}0]$  zone axis of (c, d) the multi-Ti at necking. Dislocation configurations in the deformed micro-grains were viewed with  $g = 0\bar{1}10$  and  $g = 0002$ , respectively.



**Fig. 15.** TEM images in two-beam condition near the  $[2\bar{1}10]$  zone axis of the CG-Ti at  $\sim 15\%$  strain. Dislocation configurations in the deformed micro-grains were viewed with  $g = 0\bar{1}10$  and  $g = 0002$ , respectively.



**Fig. 16.** SEM images of the fracture morphologies from (a-c) top-view and (d-e) side-view of (a, c) UFG-Ti, (b, e) multi-Ti and (c, f) CG-Ti. The inset in (e) is the enlarged view. The cavities, cracks, slip bands and shear bands were pointed by white, black, blue and yellow arrows, respectively.

consisting of high-density dislocations occur (Fig. 6a). Via intentionally chosen annealing temperature much below the recrystallization one, the UFG-Ti is hard to recrystallize. Only a small amount micro-grains are formed and the UFGs slightly coarsen and have a low dislocation density, half of UFGs still keep high-density dislocations (Fig. 5c). It is worth noting that the elongated grains evolve into micro-grains in the multi-Ti sample. In our work, the HGS multi-Ti is distinctly different from the heterostructured Ni through the same strategy reported in the literature [55]. It was revealed that the heterostructured Ni sample is microstructurally different, composed of the recrystallized CG lamellae

embedded in the UFG matrix. It was elucidated that the CGs with large grain size and the UFGs with high-density dislocations exhibits inferior combination of strength and ductility [55]. In this work, the micro-grains in the multi-Ti are only 1–4  $\mu\text{m}$ , which are fine grains, and not all UFGs have high-density dislocations. The grains in the multi-Ti can be divided three classes based on the strength difference. The micro-grains are soft domains, the recrystallized UFGs are hard domains, and the deformed UFGs with high-density dislocations can be regarded as harder domains compared with the recrystallized UFGs. It should be taken into account the inhomogeneous distribution of

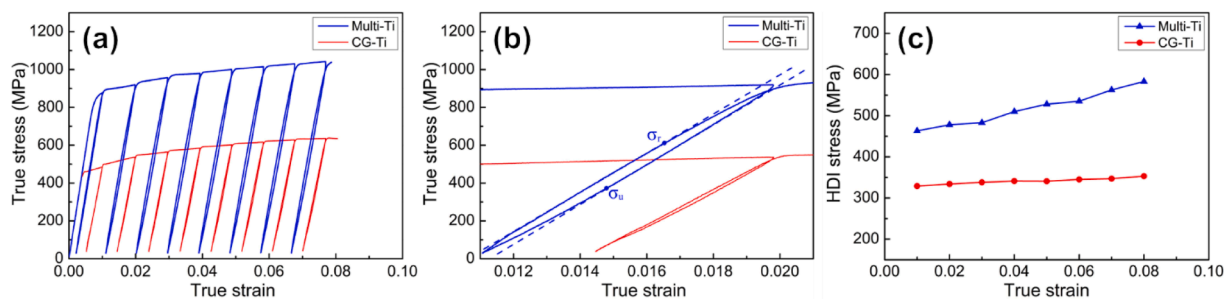


Fig. 17. (a) The LUR stress-strain curves, (b) the magnified hysteresis loops and (c) the evolution of HDI stresses with applied strain of the multi-Ti and CG-Ti, respectively.

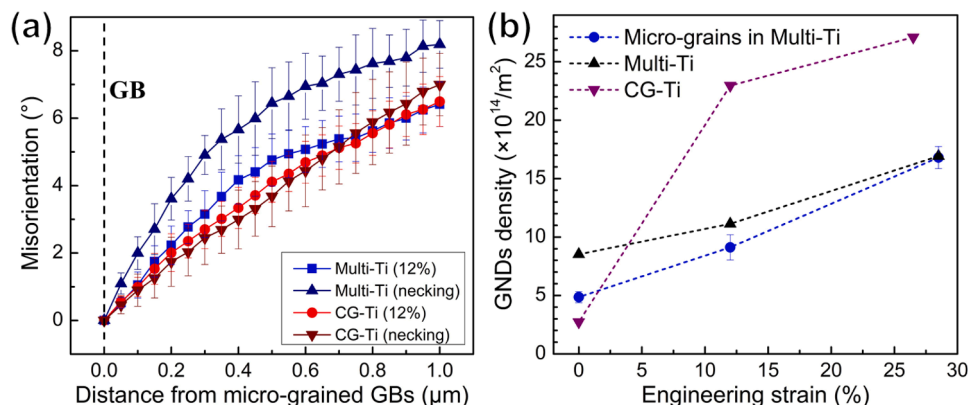


Fig. 18. (a) The misorientation gradient distribution from the GBs of micro-grains to interiors in the multi-Ti and CG-Ti at different tensile strain. (b) The evolutions of GNDs density of micro-grains in the multi-Ti, the overall areas of the multi-Ti and CG-Ti during tension.

dislocations. If high-density dislocations exist in the micro-grains and the UFGs have low-density dislocations, it may lead to small strength difference among soft/hard domains, thereby lessening the HDI hardening effect. However, if the dislocation density of the UFGs is too high, the hard domains cannot deform plastically and it is difficult for the interfaces of soft/hard domains to coordinate plastic deformation. Therefore, as long as both domains can deform plastically, the strength difference between the soft and hard domains must be maximized.

#### 4.2. HDI extra strain hardening

The multi-Ti shows distinctly different deformation mechanisms compared to the CG-Ti. Dislocation substructure and grain refinement take place in the CG-Ti under tension. Most generated GNDs form plenty of LAGBs and some HAGBs, and few GNDs produce back stresses during tensile loading. At necking, the misorientation gradient is linearly related to the distance from the GBs (Fig. 18a). These may explain that the HDI stresses in the CG-Ti increase slightly with the increased strain (Fig. 17c). While for the multi-Ti, a small quantity of LAGBs is formed and no significant grain refinement is observed during tension (Fig. 10). Furthermore, distinct strain gradient along GBs to the interior of the micro-grains exists in the multi-Ti (Fig. 18a), contributing to the high HDI stresses. Compared to the CG-Ti, the misorientation curve of the multi-Ti rises faster in the region near the GBs (about 500 nm away from GBs), indicative of a higher strain gradient. Based on the rule of mixture, the YS of the multi-Ti is estimated to be 935 MPa, higher than the measured value of 800 MPa. This is attributed to the fact that half of UFGs slightly coarsen and have low-density dislocations, as shown in Fig. 5. However, the strain hardening capacity significantly improves and the fracture elongation increases to 28.5%, comparable to the CG-Ti. The extra strain hardening stems from synergistic effect between hard (UFGs) and soft (micro-grains) domains in the multi-Ti. Dislocation

hardening and HDI hardening together contribute to the excellent strain hardening capacity of the multi-Ti.

The current study suggests that the constrained micro-grains can accommodate more strains and activate more GNDs pile-ups (e.g. extra  $\langle c + a \rangle$  dislocations) to adapt the strain gradient during tensile loading. This can be deduced from the GNDs density evolution of micro-grains with the increasing tensile strain in the multi-Ti (Fig. 18b). Before tensile testing, the GNDs density of micro-grains is  $4.8 \times 10^{14} \text{ m}^{-2}$ , much less than the overall level of the multi-Ti ( $8.5 \times 10^{14} \text{ m}^{-2}$ ). Nevertheless, with increasing tensile strain the GNDs density of micro-grains increases to  $9.1 \times 10^{14} \text{ m}^{-2}$  and then to  $1.6 \times 10^{15} \text{ m}^{-2}$ , finally catching up with the overall level. The GNDs density of micro-grains increases by  $\sim 90\%$  but the whole regions of multi-Ti only increases by  $\sim 31\%$  at the strain of  $\sim 12\%$ , and then further increases by  $\sim 85\%$  and  $\sim 52\%$  at necking, respectively. It further demonstrates that dislocation slip commences in the micro-grains at low strain stage, and then occurs synchronously in the UFGs at the late stage. The micro-grains exhibits higher growth rate of the GNDs density compared to the UFGs. In addition, high-density  $\langle c + a \rangle$  dislocations may be activated by stress concentration in the micro-grains, restrained by three-dimensional UFG matrix. Therefore, all the constrained areas in the micro-grains experience the tensile strain and overcome the deformation incompatibility in the multi-Ti by activating additional  $\langle c + a \rangle$  slip systems (Fig. 14c,d). This echoes a recent publication that the strain gradient and HDI stresses are conducive to the activation of low Schmid factor pyramidal  $\langle c + a \rangle$  slip in the HL Mg alloy with alternating fine-grained and CG layers [56]. By contrast, the CRSS anisotropy between pyramidal  $\langle c + a \rangle$  slip and  $\langle a \rangle$  slip in Ti is much lower than that in Mg due to the lower  $c/a$  axis ratio. Therefore, HDI-caused extra  $\langle c + a \rangle$  dislocations should be easier for heterogeneous Ti and its alloys as well, displaying more positive deviations from the rule-of-mixtures [56].

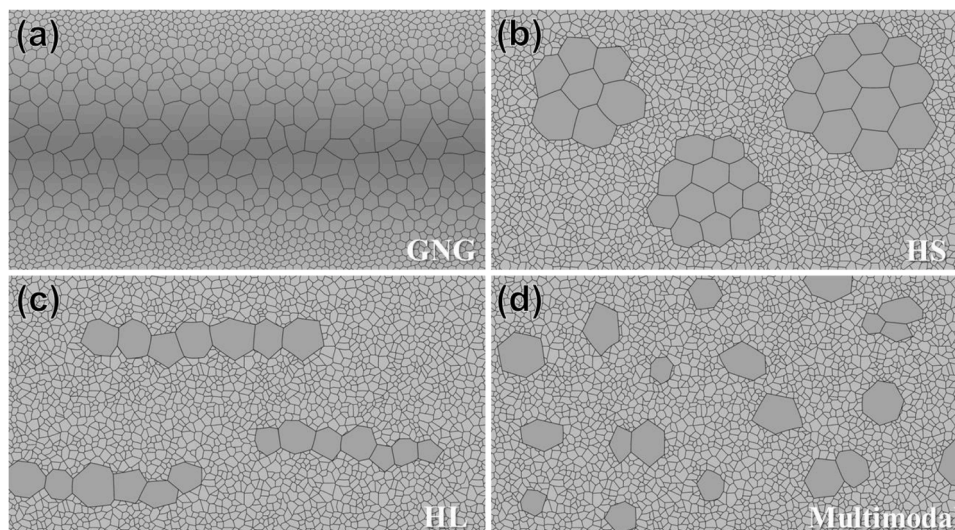


**Fig. 19.** Schematic diagrams of four typical heterogeneous grain structures: (a) Gradient nanograin (GNG) structure; (b) Harmonic structure (HS); (c) Heterogeneous lamella (HL) structure; (d) Multi-modal grain structure. Larger grains with dark gray represent micro-grains, otherwise others represent ultrafine-grains.

#### 4.3. Maximizing HDI hardening with optimal HGS

The multi-Ti displays superior combination of strength and ductility and outstanding HDI hardening effect, compared to other heterostructured Ti including GNG-Ti (gradient nanograin Ti), HS-Ti and HL-Ti (schematically shown in Fig. 19). The interpretations are twofold as follows. First, the strength elevated with the increasing volume fraction of hard domains and no obvious ductility was noticed until the soft domains exceeds a certain volume fraction to be networked [12,17,22,24]. The optimal volume fraction of the soft domains is about 30% in the HL-Ti [22]. In our work, the multi-Ti also has 30 vol% soft domains. Second, the density of interfaces between hard and soft domains differs greatly in the above four HGSs, which is decisive for the strain hardening behavior. As demonstrated above, plenty of dislocations are accumulated along zone boundaries upon tensile loading, triggering strong strain and stress gradients. It is reasonable that the spatial distributions of hard and soft domains are correlated with the interface density. Assuming that the micro-grains are hexagonal in two dimensions, the interfacial density will be one-sixth less if two micro-grains are adjacent, and one-third less if three micro-grains are adjacent. It should be pointed out that the density of interfaces in GNG structure is the lowest, thus far away from the maximum HDI strain hardening. The micro-grains are more dispersed in the multi-modal grain structure, and the density of interfaces is therefore larger, bringing out unparallel combination of strength and ductility. Pursuing the limit of the HDI hardening effect will ultimately solve the bottleneck of other UFG materials; we leave this work for the future.

## 5. Conclusions

In this work, we prepared UFG commercial pure Ti with high strength by means of ECAP processing method. A typical heterostructure with multi-modal grain structure was introduced by annealing in order to toughen the UFG-Ti sample. The dominating microstructures and deformation mechanisms at different strain stages were systematically investigated. The main conclusions are drawn as follows:

- (1) The UFG-Ti sample exhibits high strength (YS of 1100 MPa and UTS of 1210 MPa) but poor strain hardening capacity. Via annealing, a novel multi-modal grain distribution is constructed in the multi-Ti, composed of ~30 vol% recrystallized micro-grains and ~70 vol% UFGs. Half of UFGs slightly coarsen and have a low dislocation density and others still keep high-density

dislocations. The multi-Ti sample has a comparable tensile ductility (28%) with its CG counterparts (26%), a high YS of 800 MPa as well.

- (2) The micro-grains constrained by three-dimensional UFGs demand more GNDs pile-ups to accommodate the stain gradient during tensile loading. The micro-grains exhibit higher growth rate of the GNDs density compared to the UFGs in the multi-Ti sample. Numerous  $(a)$ - and  $(c + a)$ -type GNDs are arranged into dislocation arrays rather than numerous LAGBs. The continuous accumulation of GNDs plie-ups at the interfaces lead to significant increment of the HDI stresses, thereby producing enhanced HDI hardening.
- (3) The multi-Ti displays superior combination of strength and ductility and outstanding HDI hardening effect, compared to other heterostructured Ti. In addition to the volume ratio of soft/hard domains, the density of interfaces significantly affects the HDI hardening effect. The multi-modal grain structure has maximized interfacial density and therefore optimized HDI hardening consequence, which should be taken into consideration when designing ductile UFG metals.

#### Declaration of Competing Interest

The authors declare that they have no known competing financial interests or personal relationships that could have appeared to influence the work reported in this paper.

#### Acknowledgements

Y.H. Zhao and X. Chen acknowledge financial supports from the National Key R&D Program of China (Grant No. 2021YFA1200203), National Natural Science Foundation of China (Grant No. 51971112, 51225102 and 52001165), Natural Science Foundation of Jiangsu Province, China (Grant No. BK20200475) and the Fundamental Research Funds for the Central Universities (Grant No. 30919011405 and 30921011215). The authors also want to acknowledge the support of the Jiangsu Key Laboratory of Advanced Micro-Nano Materials and Technology. SEM, TEM and EBSD experiments are performed at Center of Analytical Facilities Nanjing University of Science and Technology.

#### Supplementary materials

Supplementary material associated with this article can be found, in

the online version, at doi:10.1016/j.actamat.2023.118949.

## References

- [1] A. Considère, *Annales des ponts et chaussées* 1 sem (1885) 574.
- [2] M. Legros, B.R. Elliott, M.N. Rittner, J.R. Weertman, K.J. Hemker, *Microsample tensile testing of nanocrystalline metals*, *Philos. Mag. A* 80 (2000) 1017–1026.
- [3] V.L. Tellkamp, E.J. Lavernia, A. Melmed, *Mechanical behavior and microstructure of a thermally stable bulk nanostructured Al alloy*, *Metall. Mater. Trans. A* 32 (2001) 2335–2343.
- [4] Y.H. Zhao, X.Z. Liao, S. Cheng, E. Ma, Y.T. Zhu, *Simultaneously increasing the ductility and strength of nanostructured alloys*, *Adv. Mater.* 18 (2006) 2280–2283.
- [5] G. Liu, G.J. Zhang, F. Jiang, X.D. Ding, Y.J. Sun, J. Sun, E. Ma, *Nanostructured high-strength molybdenum alloys with unprecedented tensile ductility*, *Nat. Mater.* 12 (2013) 344–350.
- [6] L. Lu, Y. Shen, X. Chen, L. Qian, K. Lu, *Ultra-high strength and high electrical conductivity in copper*, *Science* 304 (2004) 422–426.
- [7] Y.H. Zhao, J.F. Bingert, X.Z. Liao, B.Z. Cui, K. Han, A.V. Serhuceva, A. K. Mukherjee, R.Z. Valiev, T.G. Langdon, Y.T. Zhu, *Simultaneously elevating the ductility and strength of ultra-fine grained pure Cu*, *Adv. Mater.* 18 (2006) 2949–2953.
- [8] M. Bahramyan, R.T. Mousavian, D. Brabazon, *Study of the plastic deformation mechanism of TRIP-TWIP high entropy alloys at the atomic level*, *Int. J. Plast.* 127 (2020), 102649.
- [9] S. Cheng, H. Choo, Y.H. Zhao, X.L. Wang, Y.T. Zhu, Y.D. Wang, J. Almer, P.K. Liao, J.E. Jin, Y.K. Lee, *High ductility in ultrafine-grained steel via phase transformation*, *J. Mater. Res.* 23 (2008) 1578–1586.
- [10] Y. Ma, F.P. Yuan, M.X. Yang, P. Jiang, E. Ma, X.L. Wu, *Dynamic shear deformation of a CrCoNi medium-entropy alloy with heterogeneous grain structures*, *Acta Mater.* 148 (2018) 407–418.
- [11] Y. Cubides, A.I. Karayan, M.W. Vaughan, I. Karaman, H. Castaneda, *Enhanced mechanical properties and corrosion resistance of a fine-grained Mg-9Al-1Zn alloy: the role of bimodal grain structure and  $\beta$ -Mg<sub>17</sub>Al<sub>12</sub> precipitates*, *Materialia* 13 (2020), 100840.
- [12] Y.H. Zhao, T. Topping, J.F. Bingert, J.J. Thornton, A.M. Dangelewicz, Y. Li, W. Liu, Y.T. Zhu, Y.Z. Zhou, E.J. Lavernia, *High tensile ductility and strength in bulk nanostructured nickel*, *Adv. Mater.* 20 (16) (2008) 3028–3033.
- [13] Y.M. Wang, M.W. Chen, F.H. Zhou, E. Ma, *High tensile ductility in a nanostructured metal*, *Nature* 419 (2002) 912–914.
- [14] T.H. Fang, W.L. Li, N.R. Tao, K. Lu, *Revealing extraordinary intrinsic tensile plasticity in gradient nano-grained copper*, *Science* 331 (6024) (2011) 1587–1590.
- [15] K. Lu, *Making strong nanomaterials ductile with gradients*, *Science* 345 (6203) (2014) 1455–1456.
- [16] X.L. Wu, P. Jiang, L. Chen, F.P. Yuan, Y.T. Zhu, *Extraordinary strain hardening by gradient structure*, *Proc. Natl. Acad. Sci.* 111 (20) (2014) 7197–7201.
- [17] Q.S. Pan, L.X. Zhang, R. Feng, Q.H. Lu, K. An, A.C. Chuang, J.D. Poplawsky, P. K. Liaw, L. Lu, *Gradient-cell-structured high-entropy alloy with exceptional strength and ductility*, *Science* 374 (2021) 984–989.
- [18] X.L. Ma, C.X. Huang, J. Moering, M. Ruppert, H.W. Höppel, M. Göken, J. Narayan, Y.T. Zhu, *Mechanical properties of copper/bronze laminates: role of interfaces*, *Acta Mater.* 116 (2016) 43–52.
- [19] B. Gao, R. Hu, Z.Y. Pan, X.F. Chen, Y. Liu, L.R. Xiao, Y. Cao, Y.S. Li, Q.Q. Lai, H. Zhou, *Strengthening and ductilization of laminate dual-phase steels with high martensite content*, *J. Mater. Sci. Technol.* 65 (2021) 29–37.
- [20] B. Gao, Q.Q. Lai, Y. Cao, R. Hu, L.R. Xiao, Z.Y. Pan, N.N. Liang, Y.S. Li, G. Sha, M. P. Liu, H. Zhou, X.L. Wu, Y.T. Zhu, *Ultrastrong low-carbon nanosteel produced by heterostructure and interstitial mediated warm rolling*, *Sci. Adv.* 6 (2020) eaba8169.
- [21] L. Gu, R. Hou, Y. Liu, G. Chen, J. Liu, G. Zheng, R. Zhang, Y. Zhao, *Strengthening and toughening bulk Ni<sub>2</sub>CoFeV<sub>0.5</sub> medium-entropy alloy via thermo-mechanical treatment*, *J. Mater. Sci. Technol.* 151 (2023) 19–29.
- [22] X.L. Wu, M.X. Yang, F.P. Yuan, G.L. Wu, Y.J. Wei, X.X. Huang, Y.T. Zhu, *Heterogeneous lamella structure unites ultrafine-grain strength with coarse-grain ductility*, *Proc. Natl. Acad. Sci.* 112 (47) (2015) 14501–14505.
- [23] T. Sekiguchi, K. Ono, H. Fujiwara, K. Ameyama, *New microstructure design for commercially pure titanium with outstanding mechanical properties by mechanical milling and hot roll sintering*, *Mater. Trans.* 51 (2010) 39–45.
- [24] M. Ota, S.K. Vajpai, R. Imao, K. Kurokawa, K. Ameyama, *Application of high pressure gas jet mill process to fabricate high performance harmonic structure designed pure titanium*, *Mater. Trans.* 56 (2015) 154–159.
- [25] B. Sharma, M. Miyakoshi, S.K. Vajpai, G. Dirras, K. Ameyama, *Extra-strengthening in a harmonic structure designed pure titanium due to preferential recrystallization phenomenon through thermomechanical treatment*, *Mater. Sci. Eng. A* 797 (2020), 140227.
- [26] C.Y. Yu, P.W. Kao, C.P. Chang, *Transition of tensile deformation behaviors in ultrafine-grained aluminum*, *Acta Mater.* 53 (2005) 4019–4028.
- [27] Y. Zhao, T. Topping, Y. Li, E.J. Lavernia, *Strength and ductility of bi-modal Cu*, *Adv. Eng. Mater.* 13 (2011) 865–871.
- [28] M. Wang, Y. Wang, A. Huang, L. Gao, Y. Li, C. Huang, *Promising tensile and fatigue properties of commercially pure titanium processed by rotary swaging and annealing treatment*, *Materials (Basel)* 11 (2018) 1–11.
- [29] K. Wei, R. Hu, D. Yin, L. Xiao, S. Pang, Y. Cao, H. Zhou, Y. Zhao, Y. Zhu, *Grain size effect on tensile properties and slip systems of pure magnesium*, *Acta Mater.* 206 (2021), 116604.
- [30] X. Luo, Z.Q. Feng, T.B. Yu, J.Q. Luo, T.L. Huang, G.L. Wu, N. Hansen, X.X. Huang, *Transitions in mechanical behavior and in deformation mechanisms enhance the strength and ductility of Mg-3Gd*, *Acta Mater.* 183 (2020) 398–407.
- [31] Z. Zhang, J. Zhang, J. Xie, S. Liu, Y. He, K. Guan, R. Wu, *Developing a low-alloyed fine-grained Mg alloy with high strength-ductility based on dislocation evolution and grain boundary segregation*, *Scr. Mater.* 209 (2022), 114414.
- [32] T.R. Lee, C.P. Chang, P.W. Kao, *The tensile behavior and deformation microstructure of cryo-rolled and annealed pure nickel*, *Mater. Sci. Eng. A* 408 (2005) 131–135.
- [33] B.B. Wang, G.M. Xie, L.H. Wu, P. Xue, D.R. Ni, B.L. Xiao, Y.D. Liu, Z.Y. Ma, *Grain size effect on tensile deformation behaviors of pure aluminum*, *Mater. Sci. Eng. A* 820 (2021), 141504.
- [34] Y.S. Li, Y. Zhang, N.R. Tao, K. Lu, *Effect of thermal annealing on mechanical properties of a nanostructured copper prepared by means of dynamic plastic deformation*, *Scr. Mater.* 59 (2008) 475–478.
- [35] D.K. Yang, P.D. Hodgson, C.E. Wen, *Simultaneously enhanced strength and ductility of titanium via multimodal grain structure*, *Scr. Mater.* 63 (2010) 941–944.
- [36] V.V. Stolyarov, Y.T. Zhu, I.V. Alexandrov, T.C. Lowe, R.Z. Valiev, *Influence of ECAP routes on the microstructure and properties of pure Ti*, *Mater. Sci. Eng. A* 299 (2001) 59–67.
- [37] Q. Wang, J. Ren, Y. Wang, C. Xin, L. Xiao, D. Yang, *Deformation and fracture mechanisms of gradient nanograin pure Ti produced by a surface rolling treatment*, *Mater. Sci. Eng. A* 754 (2019) 121–128.
- [38] A. Fattah-alhosseini, M.K. Keshavarz, Y. Mazaheri, A.R. Ansari, M. Karimi, *Strengthening mechanisms of nano-grained commercial pure titanium processed by accumulative roll bonding*, *Mater. Sci. Eng. A* 693 (2017) 164–169.
- [39] S.V. Zherebtsov, G.S. Dyakonov, A.A. Salem, V.I. Sokolenko, G.A. Salishchev, S. L. Semiatin, *Formation of nanostructures in commercial-purity titanium via cryorolling*, *Acta Mater.* 61 (2013) 1167–1178.
- [40] S.W. Choi, C.L. Li, J.W. Won, J.T. Yeom, Y.S. Choi, J.K. Hong, *Deformation heterogeneity and its effect on recrystallization behavior in commercially pure titanium: comparative study on initial microstructures*, *Mater. Sci. Eng. A* 764 (2019), 138211.
- [41] E.W. Hart, *Theory of the tensile test*, *Acta Mater.* 15 (1967) 351–355.
- [42] Y.K. Li, F. Liu, G.P. Zheng, D. Pan, Y.H. Zhao, Y.M. Wang, *Strength scaling law, deformation kinetics and mechanisms of nanostructured Ti*, *Mater. Sci. Eng. A* 573 (2013) 141–147.
- [43] Z.W. Huang, S.B. Jin, H. Zhou, Y.S. Li, Y. Cao, Y.T. Zhu, *Evolution of twinning systems and variants during sequential twinning in cryo-rolled titanium*, *Int. J. Plast.* 112 (2019) 52–67.
- [44] S. Xu, M.Y. Gong, C. Schuman, J.S. Lecomte, X.Y. Xie, J. Wang, *Sequential {1012} twinning stimulated by other twins in titanium*, *Acta Mater.* 132 (2017) 57–68.
- [45] D.H. Shin, I. Kim, J. Kim, Y.S. Kim, S.L. Semiatin, *Microstructure development during equal-channel angular pressing of titanium*, *Acta Mater.* 51 (2003) 983–996.
- [46] M.J. Qarnia, G. Sivaswamy, A. Rosochowski, S. Boczkal, *On the evolution of microstructure and texture in commercial purity titanium during multiple passes of incremental equal channel angular pressing (I-ECAP)*, *Mater. Sci. Eng. A* 699 (2017) 31–47.
- [47] L.P. Kubin, A. Mortensen, *Geometrically necessary dislocations and strain-gradient plasticity: a few critical issues*, *Scr. Mater.* 48 (2003) 119–125.
- [48] H. Gao, Y. Huang, W.D. Nix, J.W. Hutchinson, *Mechanism-based strain gradient plasticity—I. Theory*, *J. Mech. Phys. Solids* 47 (6) (1999) 1239–1263.
- [49] M. Calcagnotto, D. Ponge, E. Demir, D. Raabe, *Orientation gradients and geometrically necessary dislocations in ultrafine grained dual-phase steels studied by 2D and 3D EBSD*, *Mater. Sci. Eng. A* 527 (2010) 2738–2746.
- [50] D.L. Zhang, H.M. Wen, M.A. Kumar, F. Chen, L.M. Zhang, I.J. Beyerlein, J. M. Schoenung, S. Mahajan, E.J. Lavernia, *Yield symmetry and reduced strength differential in Mg-2.5Y alloy*, *Acta Mater.* 120 (2016) 75–85.
- [51] M.H. Yoo, *Slip, twinning, and fracture in hexagonal close-packed metals*, *Metall. Trans. A* 12 (1981) 409–418.
- [52] L. Wang, Z. Zheng, H. Phukan, P. Kenesei, J.-S. Park, J. Lind, R.M. Suter, T. R. Bieler, *Direct measurement of critical resolved shear stress of prismatic and basal slip in polycrystalline Ti using high energy X-ray diffraction microscopy*, *Acta Mater.* 132 (2017) 598–610.
- [53] Z.X. Wu, R. Ahmad, B.L. Yin, S. Sandlöbes, W.A. Curtin, *Mechanistic origin and prediction of enhanced ductility in magnesium alloys*, *Science* 359 (2018) 447–452.
- [54] M.X. Yang, Y. Pan, F.P. Yuan, Y.T. Zhu, X.L. Wu, *Back stress strengthening and strain hardening in gradient structure*, *Mater. Res. Lett.* 4 (3) (2016) 145–151.
- [55] Y.F. Liu, Y. Cao, Q.Z. Mao, H. Zhou, Y.H. Zhao, W. Jiang, Y. Liu, J.T. Wang, Z. S. You, Y.T. Zhu, *Critical microstructures and defects in heterostructured materials and their effects on mechanical properties*, *Acta Mater.* 189 (2020) 129–144.
- [56] T. Wang, M. Zha, C. Du, H. Jia, C. Wang, K. Guan, Y. Gao, H. Wang, *High strength and high ductility achieved in a heterogeneous lamella-structured magnesium alloy*, *Mater. Res. Lett.* 11 (2023) 187–195.